

# Investigation into the Hydration Behavior of $K_2CO_3$ Packed Beds

**Citation for published version (APA):**

Raemaekers, T., Donkers, P., & Huinink, H. (2023). Investigation into the Hydration Behavior of  $K_2CO_3$  Packed Beds: An NMR Study. *Transport in Porous Media*, 149(3), 817-835. <https://doi.org/10.1007/s11242-023-01985-7>

**DOI:**

[10.1007/s11242-023-01985-7](https://doi.org/10.1007/s11242-023-01985-7)

**Document status and date:**

Published: 01/09/2023

**Document Version:**

Publisher's PDF, also known as Version of Record (includes final page, issue and volume numbers)

**Please check the document version of this publication:**

- A submitted manuscript is the version of the article upon submission and before peer-review. There can be important differences between the submitted version and the official published version of record. People interested in the research are advised to contact the author for the final version of the publication, or visit the DOI to the publisher's website.
- The final author version and the galley proof are versions of the publication after peer review.
- The final published version features the final layout of the paper including the volume, issue and page numbers.

[Link to publication](#)

**General rights**

Copyright and moral rights for the publications made accessible in the public portal are retained by the authors and/or other copyright owners and it is a condition of accessing publications that users recognise and abide by the legal requirements associated with these rights.

- Users may download and print one copy of any publication from the public portal for the purpose of private study or research.
- You may not further distribute the material or use it for any profit-making activity or commercial gain
- You may freely distribute the URL identifying the publication in the public portal.

If the publication is distributed under the terms of Article 25fa of the Dutch Copyright Act, indicated by the "Taverne" license above, please follow below link for the End User Agreement:

[www.tue.nl/taverne](http://www.tue.nl/taverne)

**Take down policy**

If you believe that this document breaches copyright please contact us at:

[openaccess@tue.nl](mailto:openaccess@tue.nl)

providing details and we will investigate your claim.



# Investigation into the Hydration Behavior of $K_2CO_3$ Packed Beds: An NMR Study

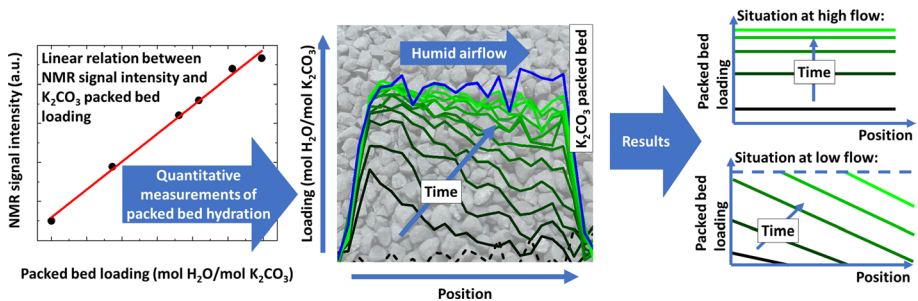
Tim Raemaekers<sup>1</sup> · Pim Donkers<sup>2</sup> · Henk Huinink<sup>1,3</sup>

Received: 17 February 2023 / Accepted: 25 June 2023 / Published online: 19 July 2023  
© The Author(s) 2023

## Abstract

$K_2CO_3$  is seen as a promising heat storage material, available for applications in the domestic sector. For practical purposes, the material is hereby often employed in a packed bed containing millimeter-sized particles. To gain more insight into the hydration behavior of these packed beds, quantitative NMR measurements, capable of following the in-situ hydration behavior, are presented for the first time. It is found that hydration behavior varies significantly, depending on the specific hydration conditions that are chosen. At low airflows hydration is found to proceed via a hydration front, while higher airflows cause the hydration front to widen. Since an increase in flow rate coincided with an increase in the supplied water vapor, hydration is eventually found to proceed in a uniform manner. A comparison between TGA and NMR measurements shows that the overall packed bed hydration kinetics hereby transition to the reaction kinetics of single  $K_2CO_3$  particles.

## Graphical Abstract



## Article Highlights

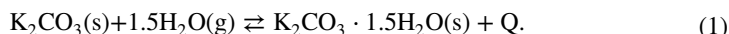
- NMR is used for the first time to quantitatively study  $K_2CO_3$  packed bed hydration
- Packed bed hydration behavior is found to be front-like for low flow rate; high flow rate results in uniform hydration
- For sufficiently high flow rates hydration kinetics are limited at single grain level

**Keywords** NMR ·  $K_2CO_3$  · Hydration · Thermochemical heat storage · Salt hydrates

## 1 Introduction

Over the past few years, solar energy harvesting has been increasingly employed, reaching a total globally installed capacity over 1 TW in the year 2022 (SolarPower Europe 2022). Mismatch between periods of high heat demand and high solar radiation does however, limit the effectiveness of solar energy harvesting in its current form (Aarts et al. 2022; Aydın et al. 2015; Beving et al. 2020; Clark et al. 2020; Donkers et al. 2017b). Heat storage is therefore necessary to increase its effectiveness (Aarts et al. 2022; Aydın et al. 2015; Beving et al. 2020; Clark et al. 2020; Donkers et al. 2017b; Houben et al. 2020; Sögütöglu et al. 2019, 2018). Different heat storage techniques like sensible, latent and thermochemical heat storage are available for this purpose (Aydın et al. 2015; Clark et al. 2020; Criado et al. 2014; Goldstein 1961; Scapino et al. 2017). Thermochemical heat storage hereby relies on the physisorption or chemisorption of a sorbent gas in a thermochemical material (TCM) (Aydın et al. 2015; Sögütöglu et al. 2018; Solé et al. 2015). Compared to other heat storage techniques it has a high energy density, combined with the ability to store heat almost loss-free over an indefinite period of time (Aydın et al. 2015; Donkers et al. 2017b; Goldstein 1961; Scapino et al. 2017; Solé et al. 2015). As a result, Goldstein already high-lighter heat storage via TCMs as a suitable option for home heating purposes in the year 1958 (Goldstein 1961).

Salt hydrates, belonging to the class of TCMs, are seen as a group of materials that is particularly suitable for applications in the domestic sector, since water vapor can be combined with it as a safe sorbate (Donkers et al. 2017b; Houben et al. 2020). Furthermore, the material group has a relatively low charging temperature suiting solar energy heat (Clark et al. 2020; Solé et al. 2015). Donkers et al. therefore performed a review on 563 hydration reactions to select salt hydrates that are available for heat storage in the domestic sector (Donkers et al. 2017b). Potassium carbonate ( $K_2CO_3$ ) was hereby selected as the most promising candidate, since it is not strongly corrosive and since the material does not have any unsafe side- or decomposition reactions. The material allows the storage/release of heat through the reversible gas–solid reaction (Donkers et al. 2017b; Sögütöglu et al. 2018):



Here the hydration reaction, going from left to right, corresponds to the exothermic discharging of the material, while the dehydration reaction from right to left corresponds to the endothermic charging of the material. The corresponding phase diagram, constructed by Sögütöglu et al., is depicted in Fig. 1 (Sögütöglu et al. 2019, 2018). Here the black solid line represents the equilibrium line, where the hydration and dehydration reaction are in equilibrium (Donkers et al. 2017b; Sögütöglu et al. 2018). Below this line the material dehydrates to its anhydrous state, resulting in a loading,  $L$  [ $\text{mol} \cdot \text{mol}^{-1}$ ], of 0 mol  $H_2O$  per mol  $K_2CO_3$ , while above the equilibrium line the material hydrates, resulting in a loading of 1.5 mol  $H_2O$  per mol  $K_2CO_3$ . These reactions do not always occur instantaneously. Close to the equilibrium line the metastable zone (MSZ) can be found, where kinetics are inhibited by a nucleation barrier (Sögütöglu et al. 2021, 2019). As a result, an induction time has to pass before the growth of a new material phase can occur.

Next to the MSZ boundaries and the equilibrium line, Fig. 1 also indicates the deliquescence line and the condensation line. Here the deliquescence line denotes another

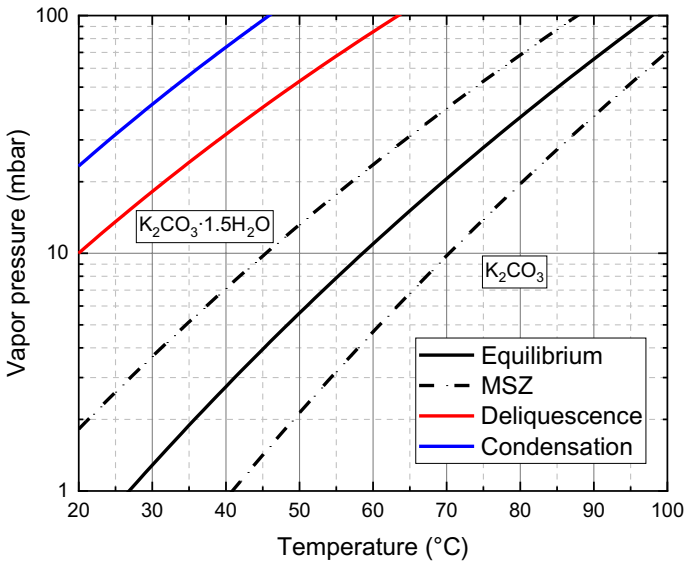


**Fig. 1** Plot of the  $K_2CO_3$  phase diagram as constructed by Sögütöglu et al. (Sögütöglu et al. 2019, 2018). The black solid line represents the  $K_2CO_3$  equilibrium line, while the red solid line indicates the material's deliquescence line. The blue solid line, indicating the condensation condition for water, is added as a reference. The metastable zones (MSZ) are indicated by the black dashed lines

phase change that hydrated  $K_2CO_3$  can undergo above certain vapor pressures. In this deliquescence phase, the salt attracts more water than it can hold inside its crystal lattice, causing the material to go into solution (Greenspan 1977; Sögütöglu et al. 2018). At even higher vapor pressure, the condensation line is reached. At these environmental conditions water vapor will condense, leading to the formation of liquid water.

To use salt hydrates like  $K_2CO_3$  in heat storage devices, they are oftentimes employed in a packed bed. Millimeter sized particles of the material are hereby poured into a reactor, creating a porous material layer with open channels (Aarts et al. 2022; Houben et al. 2020). These channels allow an airflow to be blown through the reactor, while ensuring that the pressure drop, giving rise to flow resistance does not get too high. Since the temperature and vapor pressure of the airflow entering the reactor can be controlled, a packed bed can hereby be hydrated or dehydrated in a controlled fashion. Although the application of these  $K_2CO_3$  packed beds as a heat battery seems promising, further research is necessary before commercial implementation is possible. The hydration and dehydration processes of these packed beds should for example be investigated to determine if reactions are occurring uniformly or via fronts travelling through them. After all, these reaction dynamics will determine the thermal characteristics of the salt hydrate packed beds under consideration. Furthermore, insight into the reaction dynamics of the packed beds will allow the optimization of future reactor design, allowing for more efficient thermal energy storage systems.

To investigate hydration and dehydration processes inside  $K_2CO_3$  packed beds, an imaging tool is necessary. NMR imaging is an example of a tool that is available for this purpose, since it allows non-destructively visualization of hydrogen atoms with spatial resolution (Donkers et al. 2017a, 2016, 2015). NMR studies have however shown that performing measurements on salt hydrates like  $K_2CO_3$  can be challenging due to short  $T_2$  relaxation times which give rise to fast signal decay. As a result, the

signal intensity in measurements can be low, causing a reduced signal-to-noise ratio. Donkers et al. for example, showed that structural water in  $\text{Na}_2\text{SO}_4 \cdot 10\text{H}_2\text{O}$  has a  $T_2$  relaxation time in the order of 100  $\mu\text{s}$  (Donkers et al. 2015), while lattice water in  $\text{CuCl}_2$ ,  $\text{CuSO}_4$ ,  $\text{MgCl}_2$  and  $\text{MgSO}_4$  has  $T_2$  relaxation times in the range 10 to 1000  $\mu\text{s}$  (Donkers et al. 2016).

In view of the desire to understand the reaction processes in  $\text{K}_2\text{CO}_3$  packed beds better, the goal of this study is to investigate how a packed bed containing  $\text{K}_2\text{CO}_3$  grains hydrates at different flow rates. To that end, NMR measurements are employed for the first time to quantitatively study the hydration process in  $\text{K}_2\text{CO}_3$  packed beds. To allow these measurements to take place, the signal has to be understood. NMR relaxation times are therefore first characterized as a function of  $\text{K}_2\text{CO}_3$  packed bed loading and a signal calibration is carried out. Subsequently, the quantitative NMR measurement technique is employed to study the hydration process in  $\text{K}_2\text{CO}_3$  packed beds more closely. The influence of different flow rates is hereby considered and the results found are compared to an analytical model. Furthermore, a comparison between single-grain reaction kinetics and packed bed reaction kinetics is made by comparing NMR measurements with TGA results.

## 2 Materials and Methods

### 2.1 Materials

$\text{K}_2\text{CO}_3$  grains as developed in the CREATE project are investigated in this publication (Houben et al. 2020). The grains produced by Caldic have an irregular shape and size and consist out of a mixture of hydrated potassium carbonate,  $\text{K}_2\text{CO}_3 \cdot 1.5\text{H}_2\text{O}$ , and graphite. Due to their irregular shape and size the grains were sieved into different size fractions after production. For experimentation grains in the range 1.25 mm to 3 mm and 3 mm to 5 mm are combined in a ratio of 2 to 1 to increase the bulk density of the investigated TCM beds.

Prior to the start of a hydration experiment, the sample material under investigation is dehydrated in an oven at 130 °C. The material is subsequently allowed to cool down in an enclosed container before it is poured into the NMR sample holder. To enable a comparison of different experiments the starting masses and heights of the investigated packed beds are chosen equally. Packed beds with an average height of 10.6 cm (standard deviation: 0.1 cm) are used, while the average mass is equal to 37.7 g (standard deviation: 1.1 g). The average porosity, including contributions from the packed bed filling fraction and the grain porosities itself, is calculated to be 63% (standard deviation: 1%).

### 2.2 NMR Imaging

NMR imaging is a technique with which the presence and quantity of  $^1\text{H}$  nuclei can be measured non-destructively (Donkers et al. 2017a, 2016). The technique relies on the fact that the nuclei possess a magnetic dipole moment, causing them to resonate with a frequency  $f_0$  [MHz] when placed in an external magnetic field  $\vec{B}_0$  [T] (Brown et al. 2014). The resonance frequency, called the Larmor frequency, is proportional to the strength of the external magnetic field via the gyromagnetic ratio  $\gamma$  [MHz  $\cdot$  T $^{-1}$ ]:

$$f_0 = \gamma \left| \vec{B}_0 \right|. \quad (2)$$

By utilizing the resonance property, a sample containing  $^1H$  nuclei can be measured when placed in a magnetic field. To that end, radio frequency pulses (RF pulses) have to be sent with an RF coil. The  $^1H$  nuclei subsequently emit a signal at the Larmor frequency which can be measured. Since spatially resolved measurements are often required, a gradient  $\vec{G}$  [ $T \cdot m^{-1}$ ] can be applied to the external magnetic field. The Larmor frequency then becomes position dependent, allowing an experimenter to excite and measure thin sample slices by utilizing finite bandwidth RF pulses (Brown et al. 2014):

$$f_0(x) = \gamma \left( \left| \vec{B}_0 \right| + \left| \vec{G} \right| x \right). \quad (3)$$

In this publication, the slice-selective Hahn spin echo sequence is used to perform spatially resolved quantitative NMR measurements on  $K_2CO_3$  packed beds (Brown et al. 2014). A schematic overview of this pulse sequence can be seen in Fig. 2.

In this pulse sequence, a hard  $90^\circ$  RF pulse, which has a pulse duration  $t_p$  [ $\mu s$ ], is combined with a hard  $180^\circ$  pulse which has an equal length, but twice the power. As a result, an echo is formed at the echo time  $t_e$  [ $\mu s$ ]. The time interval  $WW$  [s] indicates the time window in which this echo is acquired. To improve the signal-to-noise ratio in the experimental data, measurements can be repeated and averaged. The different measurements are hereby separated by the repetition time  $t_r$  [ms]. During the entire measurement procedure, a gradient  $G$  [ $T \cdot m^{-1}$ ] is engaged. Its purpose is to excite sample slices with a well-defined thickness  $\Delta l$  [mm], given by the equation:

$$\Delta l = \frac{1}{G \cdot \gamma \cdot t_p}. \quad (4)$$

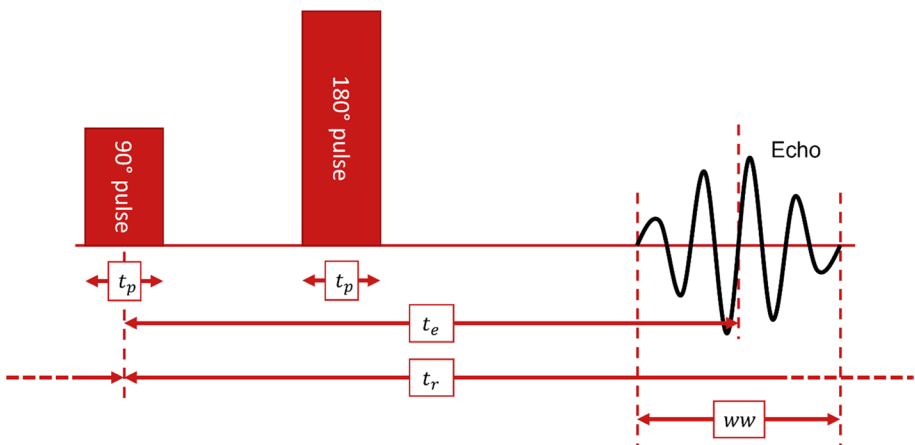


**Fig. 2** Schematic representation of the Hahn spin echo sequence that is used for the measurements in this publication. A  $90^\circ$  and  $180^\circ$  RF pulse with time duration  $t_p$  are applied to form an echo at the echo time,  $t_e$ . The echo is hereby measured during a time window indicated as the window width,  $WW$ . To improve the signal-to-noise ratio of the results, measurements are repeated and averaged. The different measurements are hereby separated by the repetition time,  $t_r$

To construct a 1D image of an investigated sample, slice-selective Hahn-spin echo measurements have to be performed at regular position intervals along one of the sample's axis. The Fourier transform should subsequently be applied to each of the individual measurements to determine the signal intensity at the Larmor frequency. By plotting the signal intensities found as a function of position, a sample profile or 1D image is hereby obtained. Note that the signal intensity found at each of the positions depends on the local density of the hydrogen nuclei, as well as their relaxation times. Since nuclei experiencing different mobilities can be present in a sample, the total signal intensity  $S$  [a.u.] should be split up in contributions from the different species  $i$ . The resulting signal equation then becomes (Brown et al. 2014):

$$S \propto \sum_i \rho_{H,i} \exp\left(-\frac{t_e}{T_{2,i}}\right) \left(1 - \exp\left(-\frac{t_r}{T_{1,i}}\right)\right), \quad (5)$$

where  $\rho_{H,i}$  represents the density of the  $^1\text{H}$  protons in species  $i$  and where  $T_{1,i}$  and  $T_{2,i}$  represent their respective longitudinal and transversal relaxation times. To ensure a sufficiently high signal in NMR measurements, the repetition time should be at least 4 times as high as the longest  $T_1$  time that is encountered. Furthermore, Hahn spin echoes should be acquired with an echo time that is sufficiently short to prevent too much signal decay due to  $T_2$  relaxation.

### 2.3 Hydration Experiments

A schematic overview of the NMR setup used in the hydration experiments of  $\text{K}_2\text{CO}_3$  packed beds can be seen in Fig. 3.

The NMR system has a main magnetic field of 0.80 T, causing  $^1\text{H}$  nuclei to resonate with a frequency of 33.89 MHz. To allow quantitative measurements to take place,  $90^\circ$  and  $180^\circ$  RF pulses with a duration of  $30 \mu\text{s}$  are sent with a solenoid containing a Faraday shield. The solenoid has a height of approximately 25 mm and is constructed around a Teflon tube with a bore diameter of 30 mm. Hahn spin echo measurements are taken with an echo time and window width of  $250 \mu\text{s}$  and  $200 \mu\text{s}$  respectively. Each measurement point is hereby averaged 16 times to improve signal-to-noise ratio. The repetition time in between these measurements is equal to 1.5 s. To allow slice-selection to take place, a gradient with a strength of  $10.42 \text{ kHz} \cdot \text{mm}^{-1}$  is engaged during the measurements. According to Eq. (4), the selected gradient strength and pulse duration therefore result in excited sample slices of 3.2 mm.

The NMR setup contains a stepper motor from which a cylindrical reactor can be suspended. During hydration experiments, a Teflon reactor with an inner diameter of 22 mm is used. It is able to accommodate packed beds with a height up to 166 mm. Glass filters are placed at the top and bottom of the reactor to keep the sample material in place and to ensure a free flow of air. To hydrate the  $\text{K}_2\text{CO}_3$  bed during experiments, a home-built humidifier is connected to the reactor. The humidifier can generate an airflow between 0 and  $10 \text{ L} \cdot \text{min}^{-1}$  with a humidity between 0 and 29.7 mbar. Sensirion SHT85 Temperature & Humidity sensor are placed at the reactor in- and outlet. They measure temperature and humidity with a typical accuracy of  $0.1 \text{ }^\circ\text{C}$  and 1.5% RH respectively (Sensirion 2021).

In a hydration experiment, the dehydrated  $\text{K}_2\text{CO}_3$  grains are poured into the reactor to create a packed bed. A dry airflow of  $10 \text{ L} \cdot \text{min}^{-1}$  is subsequently blown through the reactor to prevent hydration, while the starting condition of the packed bed is measured. A 1D

**Fig. 3** Schematic overview of the NMR setup. The reactor accommodating the investigated packed bed is suspended inside the setup with a stepper motor, while an air supply blows an airflow, set to the desired flow rate and vapor pressure through it. Spatially resolved, quantitative NMR measurements are achieved by using an RF coil with a Faraday shield and by combining the measurements with a 1D gradient in the main magnetic field

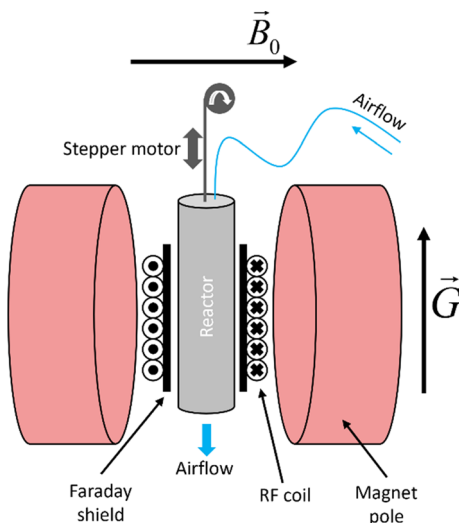


image of the packed bed is hereby obtained by measuring slice-selective Hahn spin echo measurements at regular position intervals along the reactor's longitudinal axis. The stepper motor is hereby used to move the reactor through the NMR setup. Following the measurement of the packed bed's initial stage, the airflow is switched to the desired humidity and flow rate to start the hydration process. Scans of the reactor are hereby continuously made by moving the reactor up and down through the NMR setup. A full scan of the reactor is hereby achieved in approximately 45 min. Next to NMR measurements, temperature and humidity data are also gathered during the hydration experiments. A measurement is hereby taken together with every NMR measurement.

Since the NMR measurements are performed in a step-by-step fashion, the loading that is measured in each layer of the  $K_2CO_3$  packed bed corresponds to a different moment during the hydration experiment. To make sure that the results from the experiments can be interpreted more easily, the data are time interpolated. As a result, the hydration profiles resulting from the NMR experiments all correspond to a single moment in time.

## 2.4 NMR Signal and Loading

As was illustrated by Eq. (5), both the  $T_1$  and  $T_2$  relaxation time directly influence the signal that is measured in an NMR experiment. This section therefore focusses on determining the  $T_1$  and  $T_2$  relaxation time as a function of packed bed loading, as well as calibrating the NMR signal. To that end calibration samples consisting out of fine  $K_2CO_3$  crystals are investigated. These samples are prepared such that they have different fractions of hydrated material. As a consequence, the effective loading of the samples varies between  $L = 0$  and  $L = 1.5$ . To create the calibration samples  $K_2CO_3 \cdot 1.5H_2O$  is dehydrated inside an oven at  $130^\circ C$ . The samples are subsequently poured into the sample holder for experimentation.

To measure the  $T_1$  relaxation time of the calibration samples the saturation recovery sequence is used (Arnold 2007; Nicasy et al. 2022). Results indicate that all samples have a  $T_1$  relaxation time between 250 and 350 ms. In Sect. 2.2 it is indicated that a repetition time of at least 1.4 s should therefore be used during hydration experiments. As was indicated in Sect. 2.3, the repetition time in all experiments is equal to 1.5 s, satisfying this requirement.



$T_2$  relaxation times of the samples are measured using the CPMG sequence with an echo time of 250  $\mu\text{s}$  (Brown et al. 2014). It is found that the samples have an approximately constant relaxation time in the sub-millisecond scale. This timescale corresponding to the interval of relaxation times previously indicated by Donkers et al. to belong to structural or lattice water in different types of salt hydrates (Donkers et al. 2016, 2015). A full overview of the  $T_1$  and  $T_2$  relaxation time measurements, as well as a discussion on the measurement results can be found in the appendix.

Following the determination of the  $T_1$  and  $T_2$  relaxation characteristics of  $\text{K}_2\text{CO}_3$  packed beds, the signal calibration is carried out. To that end, the calibration samples are poured into the Teflon sample holder introduced in Sect. 2.3. Hahn spin echo measurements are subsequently taken at different positions along the axial direction of the created packed beds and the signal intensities found at these different positions are averaged. Plotting the resulting values as a function of sample loading Fig. 4 is found. Here it can be seen that the NMR signal intensity depends linearly on the loading of the  $\text{K}_2\text{CO}_3$  calibration samples. This can be understood by considering Eq. (5), which indicates that the NMR signal intensity should scale linearly with  $^1\text{H}$  proton density. After all, the  $T_2$  relaxation times of the calibration samples are approximately constant as a function of sample loading. Since the  $\text{K}_2\text{CO}_3$  calibration samples have experienced limited changes in density during their preparation, the proton density here is approximately equivalent to sample loading, explaining the linear correlation between NMR signal and sample loading found in Fig. 4. Note that it can also be observed in the figure that the signal intensity of a completely anhydrous sample is not equal to zero. The noise baseline of the NMR instrument can be indicated as the cause for this behavior.

Now it has been shown that the signal of a  $\text{K}_2\text{CO}_3$  sample depends linearly on its loading, an arbitrary measurement signal can simply be transformed into a loading. To that end, the constant noise baseline of the NMR machine is taken to correspond with a completely

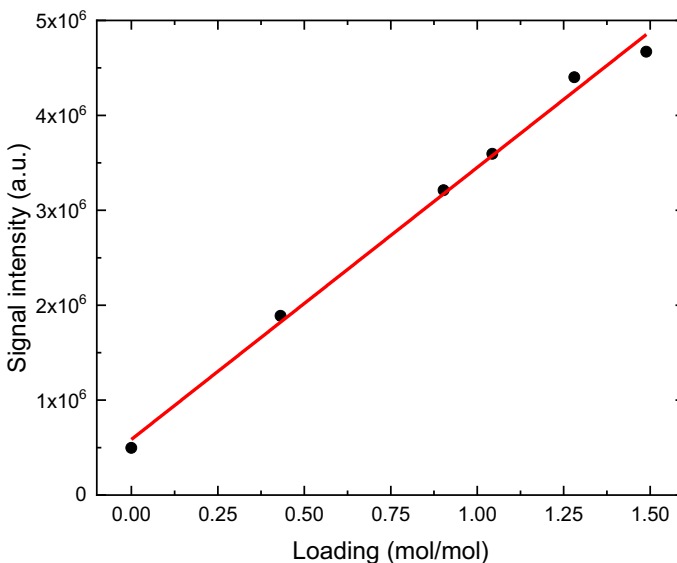


**Fig. 4** Calibration plot illustrating the linear relationship between NMR signal intensity and packed bed loading in mol  $\text{H}_2\text{O}$  per mol  $\text{K}_2\text{CO}_3$

anhydrous sample, while the maximum average signal intensity, which is found in the measurement under consideration, should be coupled to a fully hydrated sample. The loading of partially hydrated  $K_2CO_3$  material can then be calculated using the linear relation between signal intensity and loading. Note that it is hereby implicitly assumed that the filling fraction of the  $K_2CO_3$  packed bed is uniform along its axial direction, since the maximum average signal intensity is coupled to a fully hydrated sample.

## 2.5 TGA Experiments

Single grain  $K_2CO_3$  hydration measurements are conducted with a Mettler-Toledo TGA/DSC 3+, connected to a home-built humidifier. The humidifier blows a nitrogen flow with the desired relative humidity through the TGA, allowing precise in situ measurements of sample mass, while hydration occurs with a well-defined vapor pressure and temperature. TGA temperature can be regulated with an accuracy of 0.3 °C, while mass measurements are taken with a resolution of 0.1  $\mu\text{g}$ . The flow rate of the humidifier is fixed at 0.3  $\text{L} \cdot \text{min}^{-1}$ . Vapor pressure and temperature were both calibrated prior to experiments using the methodology of Sögütoglu et al. (Sögütoglu et al. 2018, 2019, 2021).

In a hydration experiment, the  $K_2CO_3$  grains are first brought to their anhydrous state by applying a humidity of 8 mbar (0.2%RH) with a temperature of 140 °C. Conditions are maintained until a stable thermogravimetric signal is obtained, corresponding to a fully anhydrous sample. Hydration is subsequently performed by exposing the sample to a humidity of 8 mbar (25.2%RH) and a temperature of 25 °C.

## 3 Results

Quantitative NMR measurements are now employed to study the hydration behavior of  $K_2CO_3$  packed beds under different experimental conditions. First, the results of a typical hydration experiment are discussed in more detail. Amongst other things, it is hereby explained how the hydration profiles obtained by the NMR setup should be interpreted. Subsequently, the hydration behavior of  $K_2CO_3$  packed beds is studied as a function of flow rate. The changes in the observed front widths are hereby coupled to the theory of an analytical model. Finally, the hydration kinetics measured in the experiments with different flow rates are studied and compared to single-grain hydration kinetics which are observed in TGA measurements.

### 3.1 Water Distribution During Hydration

Quantitative NMR imaging can now be employed to study the hydration behavior of  $K_2CO_3$  packed beds under different experimental conditions. First, the results of a typical measurement at a water vapor pressure of 8 mbar (27.6% RH at a lab temperature of 23.5 °C) and a flow rate of 0.4  $\text{L} \cdot \text{min}^{-1}$  are discussed in more detail. The sample is prepared following the procedure described in Sect. 2.1. Loading profiles which illustrate the course of the hydration process are shown in Fig. 5. Here the left-hand side of the profiles corresponds with the top of the investigated packed bed, while the right-hand side indicates its bottom. The airflow which is used in the experiment is blowing through the reactor from top to bottom. Its direction is indicated by the blue horizontal arrow in the figure. The

measurement of a single hydration scan takes approximately 45 min, but to improve clarity of the figure a loading profile is only shown every 12 h.

Investigating the experimental results it can be seen that the black dashed line, corresponding to the initial reactor scan, shows a loading of approximately  $0 \text{ mol} \cdot \text{mol}^{-1}$  throughout the entire packed bed. As expected, the  $\text{K}_2\text{CO}_3$  material inside the reactor is therefore confirmed to be in its anhydrous state at the start of the experiment. After this initial reactor scan, the applied airflow is switched to the desired settings for the hydration experiment and the  $\text{K}_2\text{CO}_3$  packed bed is continuously measured. As can be seen, hydration occurs via a hydration front that travels through the  $\text{K}_2\text{CO}_3$  packed bed in the direction of the applied airflow. When the hydration level in a  $\text{K}_2\text{CO}_3$  layer approaches the maximum value of  $1.5 \text{ mol} \cdot \text{mol}^{-1}$ , the hydration process slows down, causing the hydration front to become increasingly shallower as time progresses. After 6 days of hydration the packed bed is almost completely hydrated and the loading profiles only show a marginal difference with respect to each other. These profiles are therefore not plotted in Fig. 5. Instead, the loading profile that was measured in the last scan of the experiment is plotted. It is indicated by the blue solid line.

Although the loading of  $\text{K}_2\text{CO}_3$  salt can only attain a value of 0 or  $1.5 \text{ mol} \cdot \text{mol}^{-1}$  at the crystalline level, the loading profiles in Fig. 5 are found to vary continuously in between these two values. The hydration kinetics of the individual particles that make up the packed bed can be identified as the cause of this behavior. As was described in the work of Aarts et al., the hydration kinetics of these salt particles is diffusion limited, causing the hydration process to occur via a hydration front that travels into the grain (Aarts et al. 2022). Consequently, the overall loading of a  $\text{K}_2\text{CO}_3$  particle, or a layer inside the investigated packed bed can assume an overall loading varying in between 0 to  $1.5 \text{ mol} \cdot \text{mol}^{-1}$ .

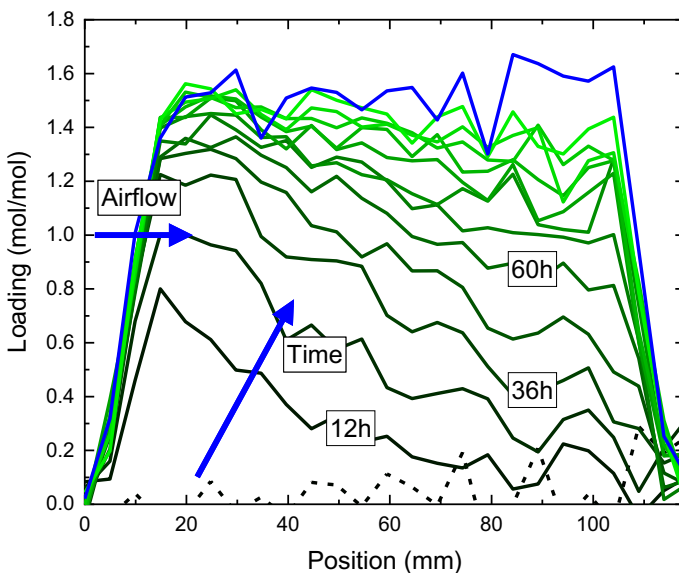


**Fig. 5** Hydration of a packed bed, consisting out of  $\text{K}_2\text{CO}_3$  particles, with an airflow of  $0.4 \text{ L} \cdot \text{min}^{-1}$  at a vapor pressure of 8 mbar. The airflow blows through the reactor from top to bottom, indicated by the blue horizontal arrow. Loading profiles are separated by time intervals of 12 h. The dashed line indicates the loading profile from the initial reactor scan, while the solid lines represent the hydration process. The final loading profile, measured at the end of the hydration process, is indicated by the blue line

To study the hydration process of the  $K_2CO_3$  packed bed more closely it is insightful to compare the hydration level of different packed bed layers as a function of time. The hydration level at positions 25 mm, 59 mm and 94 mm are therefore plotted as a function of time in Fig. 6A. As can be seen, the initial hydration rates of the different layers inside the packed bed are not constant. Instead, it is found that the hydration rate decreases for positions deeper inside the reactor. This behavior can be explained by considering the water vapor pressure of the airflow, plotted in Fig. 6B. Here it can be seen that the water vapor pressure at the outflow of the reactor is unequal to the inflow vapor pressure during a significant portion of the hydration process. As a result, it must be concluded that the vapor pressure inside the packed bed has a gradient, leading to a decrease in humidity for positions deeper inside the reactor. It can therefore be anticipated that hydration kinetics inside the  $K_2CO_3$  packed bed are fastest near the reactor's inlet and decrease for position deeper inside of it. After all, single jump experiments performed by Beving et al. showed that hydration kinetics of  $K_2CO_3$  powder beds are increased when water vapor pressure is increased (Beving et al. 2022), while Aarts et al. showed that power output and therefore the hydration kinetics of cylindrical  $K_2CO_3$  particles increases when hydration is performed at higher water vapor pressures (Aarts et al. 2022).

Another observation which can be made from Fig. 6B is that the measured water vapor pressure at the reactor outflow remains approximately constant at a value of 2 mbar (5.6%RH at 27 °C) during the initial stage of the hydration experiment. This effect can be explained, since the hydration profiles have not yet reached the end of the packed bed during this period. As a result, the packed bed can absorb water vapor until reaction conditions corresponding closely to the MSZ line are reached (Sögütöglu et al. 2019). For the conditions in this experiment it is found that the outflow temperature of the reactor is approximately equal to 27 °C. Figure 1 indicates that the water vapor pressure corresponding to the MSZ line should therefore be equal to 3.0 mbar (8.4%RH at 27 °C). This is in reasonable agreement with the 2 mbar (5.6%RH at 27 °C) water vapor pressure found in the experimental data, considering the fact that accuracy of such measurements decreases at lower water vapor pressures.

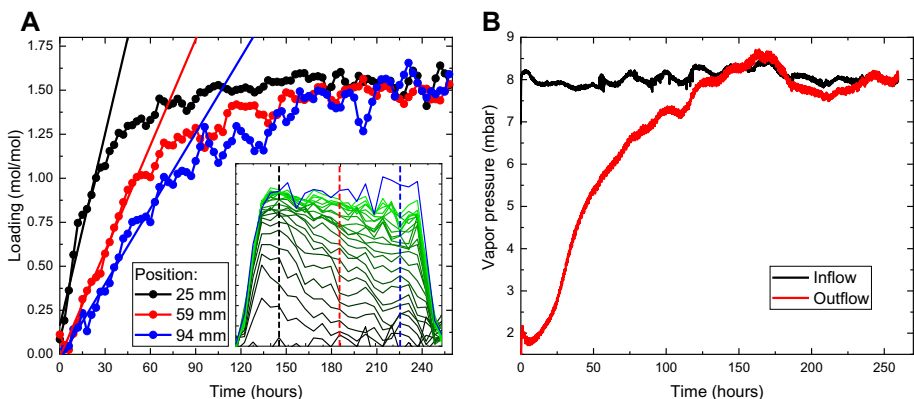


**Fig. 6** **A** Plot of the hydration level at positions 25 mm, 59 mm and 94 mm as a function of time. Linear fits are made through the data point in between hydration levels of  $0 \text{ mol} \cdot \text{mol}^{-1}$  and  $1 \text{ mol} \cdot \text{mol}^{-1}$ . The inset shows the original loading profiles together with the investigated positions. **B** Plot of the water vapor pressure measured at the reactor in- and outflow

### 3.2 Hydration in Relation to Flow Rate

Experiments at different flow rates can now be compared to each other to determine the influence that flow rate has on the hydration behavior of  $K_2CO_3$  packed beds. Experiments that are compared were conducted at a water vapor pressure of 8 mbar (27.6%RH at a lab temperature of 23.5 °C) and flow rates of 0.4, 1.0, 2.3 and 8.7  $L \cdot \text{min}^{-1}$ . The loading profiles belonging to these different experiments are plotted in Fig. 7. The respective loading profiles have a time interval of 3 h in between each other.

Comparing the different plots it can be seen that the width of the hydration front in figures A to C increases as the flow rate is raised. An effect like this can be anticipated, since the flux of water vapor entering the reactor becomes larger when the flow rate is increased, while the single-grain reaction kinetics remain approximately constant. After all, the temperature and vapor pressure of the applied airflow is kept constant in each experiment. An explanation for this behavior can also be found in the work of Huinink et al., where a theoretical model, describing the isothermal hydration process in a packed bed is formulated (Huinink et al. 2023). Here it is found that the width of a hydration front traveling through an infinitely long packed bed increases when the average air velocity in the packed bed,  $U$  [ $\text{m} \cdot \text{s}^{-1}$ ], is elevated:

$$W \approx C_n \left( \frac{\phi}{1-\phi} \right) \frac{r^2 U}{D}. \quad (6)$$

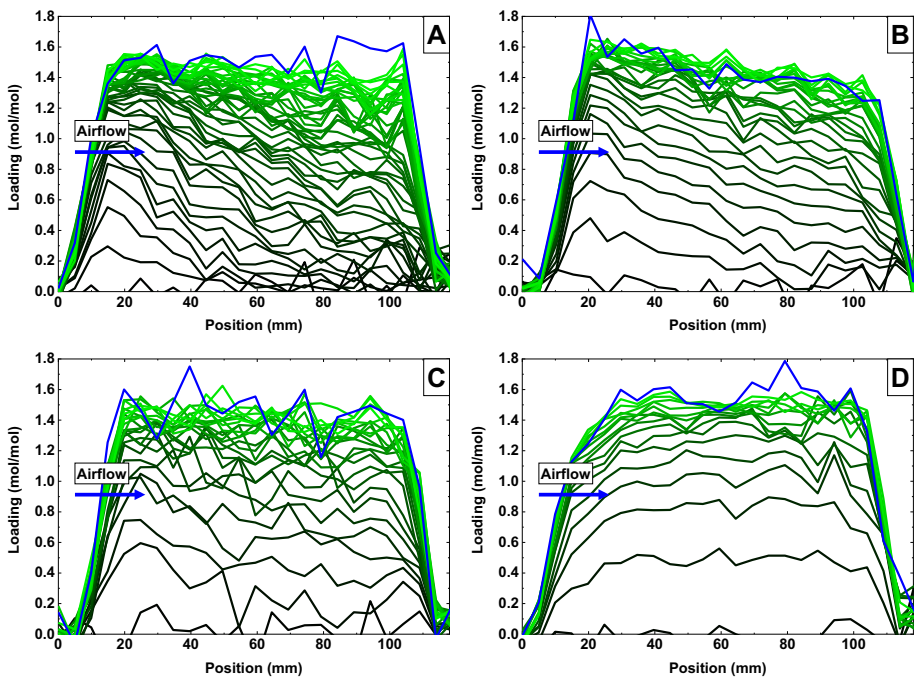


**Fig. 7** Loading profiles belonging to hydration experiments at different flow rates: **A** 0.4  $L \cdot \text{min}^{-1}$ ; **B** 1.0  $L \cdot \text{min}^{-1}$ ; **C** 2.3  $L \cdot \text{min}^{-1}$ ; **D** 8.7  $L \cdot \text{min}^{-1}$ . The time interval between the respective loading profiles is 3 h

The model also shows that front width  $W$  [m] depends on the packed bed porosity  $\phi$  [–] and the particles that make up the packed bed. Properties that hereby play a role are their size  $r$  [m], the diffusivity of water vapor inside of them,  $D$  [ $m^2 \cdot s^{-1}$ ], and a constant  $C_n$  [–], which is a geometry-dependent factor associated with the hydration process inside the particles ( $C_n \approx 0.25$  for spherical particles). Similar expressions have been derived for a different, but analogous problems. An example is the analytical model, developed by Gerber et al., to describe the deposition process of colloidal particles in an infinitely long porous medium (Gerber et al. 2020).

Investigating Fig. 7 further, it can be seen that in figure D the hydration process proceeds in a uniform manner without the presence of a hydration front. The flow rate has become so high that the hydration process is no longer limited by the supply of water vapor. Using Eq. (6), an estimate can be made on the front width that can be expected in this situation. Assuming typical values for the involved parameters and using the average properties of the investigated packed beds ( $C_n \approx 0.25$ ,  $\phi \approx 0.63$ ,  $r \approx 1.375$  mm,  $U \approx 0.6$  m  $\cdot$  s $^{-1}$ ,  $D \approx 1$  mm $^{-1}$  s $^{-1}$  (Aarts et al. 2022)), the front width in this situation can be estimated to be approximately 0.5 m. This front width significantly exceeds the packed bed length, explaining why uniform hydration is observed.

Since the uniform hydration process in Fig. 7D indicates that the hydration rate has become constant over the whole reactor, it can be expected that the water vapor pressure inside the reactor no longer has a significant gradient during the course of the hydration process. Investigating the vapor pressure measurements belonging to the experiment at flow rate 8.7 L  $\cdot$  min $^{-1}$ , it can indeed be seen that such results are found in the experiment. The data, plotted in Fig. 8, shows that the outflow vapor pressure quickly rises to a value similar to the inflow vapor pressure at the start of the experiment. Both vapor pressures lie within 1 mbar of each other within a time period of 3.5 h. To compare the timescale of the change in outflow vapor pressure to the total timescale of the hydration experiment, the average packed bed loading is also plotted as a function of time in Fig. 8.

### 3.3 Packed Bed & Single Grain Hydration Kinetics

To investigate the differences between the experiments at different flow rates more closely, plots of the average loading are presented as a function of time in Fig. 9. As can be expected, it is found that the reaction rate in the investigated packed beds increases when the flow rate is raised. After all, the flux of water vapor entering the reactor is linearly dependent on the chosen flow rate. For low flow rates, this means that the overall hydration rate of the  $K_2CO_3$  packed bed is limited by the supply of water vapor and not by the hydration kinetics of the individual grains. For higher flow rates the reverse is true: Here the supply of water vapor is increasingly less limiting to the overall hydration rate as the flow rate is raised. Finally, when uniform hydration is reached in the experiment at flow rate 8.7 L  $\cdot$  min $^{-1}$ , kinetics are no longer limited by the supply of water vapor. Instead, hydration rate is fully determined by the individual grains that make up the  $K_2CO_3$  packed bed. Consequently, a further increase in flow rate would not lead to a raise in the overall hydration rate of the packed bed.

The results in Fig. 9 are also compared with data from two single-grain hydration experiments conducted in the TGA. Data are hereby obtained by hydrating the separate grains inside the TGA at a temperature and vapor pressure of 25 °C and 8 mbar (25.2%RH) respectively. Since the  $K_2CO_3$  grains are irregular in shape and size, the two hydration curves do not match each other exactly. Furthermore, the exact transport mechanisms

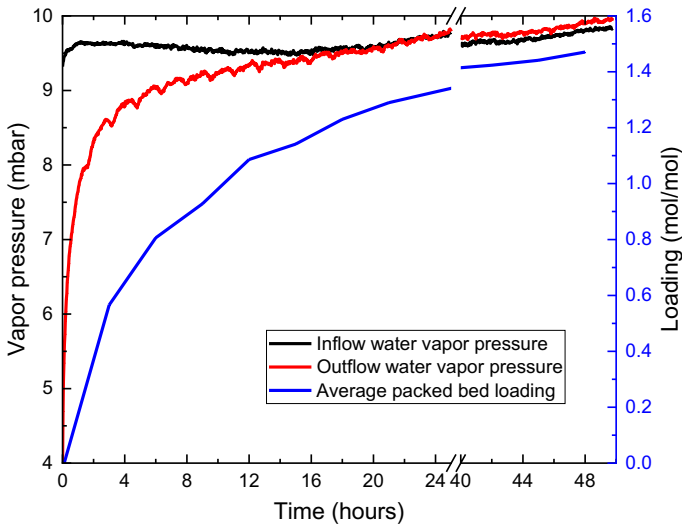


**Fig. 8** Plot of the water vapor pressure measured at the reactor in- and outflow during the hydration experiment at flow rate  $8.7 \text{ L} \cdot \text{min}^{-1}$ . The average packed bed loading is also plotted in the figure to compare the timescale of changes in the outflow vapor pressure to the total timescale of the hydration experiment

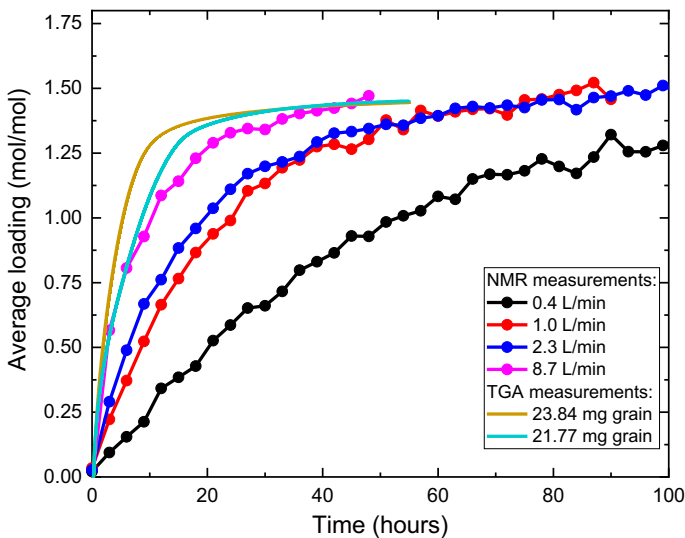


**Fig. 9** Plot of the average packed bed loading as a function of time for the experiments conducted at different flow rates. Data from two TGA experiments, conducted on single  $\text{K}_2\text{CO}_3$  grains, are added as a reference

involved in the hydration process of the particles are not taken into consideration. Nevertheless, the presented hydration curves give a good indication of the single-grain hydration kinetics at these specific experimental conditions. Comparing the hydration curves of the TGA measurements to those of the NMR experiments, it can be seen that the hydration



kinetics of single  $K_2CO_3$  grains match the average hydration rate of a  $K_2CO_3$  packed bed at a flow rate of  $8.7 \text{ L} \cdot \text{min}^{-1}$ . The experimental results therefore confirm that the hydration kinetics of a packed bed coincide with the hydration kinetics of single particles when hydration is occurring in a uniform manner.

The dependence of overall packed bed hydration rate on flow rate, presented in Fig. 9, also has an impact on the temperature lift that can be measured at the reactor outflow during the different hydration experiments. After all, the reaction enthalpy associated with the hydration of  $K_2CO_3$  is constant (Donkers et al. 2017b), indicating that experiments at increasingly higher airflows generate incrementally larger thermal powers, as long a uniform hydration has not yet been reached. Consequently, the hydration experiments performed at flow rates of  $2.3 \text{ L} \cdot \text{min}^{-1}$  and  $8.7 \text{ L} \cdot \text{min}^{-1}$  are found to result in peak temperature lifts of approximately  $3 \text{ }^\circ\text{C}$  and  $5 \text{ }^\circ\text{C}$  respectively, while hydration experiments at airflows of  $0.4$  and  $1.0 \text{ L} \cdot \text{min}^{-1}$  are not found to result in observable temperature lifts. It can however be argued that the lack of thermal insulation in the used experimental setup is most likely affecting the temperature measurements, most notably at lower flow rates. An in-depth analysis of the thermal output of the investigated packed beds is therefore beyond the scope of this publication.

## 4 Conclusion

In this publication, the hydration behavior of packed beds containing  $K_2CO_3$  grains is investigated at different flow rates. To that end, NMR imaging is performed to quantitatively measure the in-situ hydration process in these packed beds. The hydration kinetics observed in packed bed hydration experiments are hereby also compared with single grain hydration kinetics, observed in TGA experiments.

Calibration measurements show that the signal intensity, observed in an NMR measurement, scales linearly with packed bed loading. Consequently, the signal intensity observed in a hydration experiment can be converted into a packed bed loading by knowing the signal of a fully hydrated packed bed, as well as the noise baseline of the NMR machine. The loading of partially hydrated material can then be calculated with its linear relation to signal intensity.

Hydration experiments show that hydration of a  $K_2CO_3$  packed bed can occur via a hydration front, or in a uniform manner, depending on the specific flow rate that is chosen. Low airflow results in sharp hydration fronts that travel through the packed bed in the direction of the applied airflow. The water vapor pressure, measured at the outflow of the packed bed, is hereby found to be close to the edge of the MSZ, as long as the hydration front has not yet reached the end of the packed bed. Since this means that the inflow and outflow vapor pressure differ significantly during this period, a gradient in water vapor pressure can be expected to form itself inside the packed bed during the initial phase of the hydration experiment. Consequently, it is found that the packed bed hydration rate is higher at the reactor inflow, compared to the reactor outflow.

For hydration experiments at increased flowrates it is found that the hydration fronts become wider. After all, an increase in flow rate coincides with an increase in the supply of water vapor that is introduced to the packed bed, while the single-grain hydration kinetics can be anticipated to remain constant. An analytical model describing isothermal hydration of an infinitely long packed bed is compared to the experimental data. The model is found to predict the same front widening at increasing flow rates, observed in the different



hydration experiments. At a sufficiently high flow rate the hydration process is even found to progress in a uniform manner, rather than via a hydration front. The overall hydration kinetics of the investigated packed bed are hereby found to coincide with the kinetics of single  $\text{K}_2\text{CO}_3$  grains, indicating that the packed bed hydration kinetics are no longer limited by the supply of water vapor. Since the hydration rate in the different layers of the reactor should be equal in this measurement, it is found that a strong gradient in vapor pressure cannot occur inside the packed bed. As a result, the inflow vapor pressure rapidly rises to a value close to the inflow vapor pressure at the start of the hydration experiment.

In future research, the investigations into  $\text{K}_2\text{CO}_3$  packed beds could be expanded by including the effect of water vapor pressure in the analysis of the hydration behavior. In this way, the hydration behavior and kinetics could be further investigated and a more elaborated overview of  $\text{K}_2\text{CO}_3$  packed bed hydration processes can be created. Furthermore, the thermal output of these packed beds could be studied by employing a separate insulated reactor outside of the NMR setup and by performing thermal measurements inside of the packed bed itself. In this way, in-situ temperature measurements can be obtained and the insight into the thermal performance of  $\text{K}_2\text{CO}_3$  packed beds can be improved.

## Appendix

As is indicated by Eq. (5), the signal intensity in an NMR measurement is significantly affected by the  $T_1$  and  $T_2$  relaxation time of an investigated sample. This section therefore focuses on determining the  $T_1$  and  $T_2$  relaxation characteristics of  $\text{K}_2\text{CO}_3$  salt as a function of loading. To that end, the calibration samples introduced in Sect. 2.4, are poured into polypropylene sample tubes to form packed beds suitable for characterization.

To measure the  $T_1$  relaxation time of the calibration samples the saturation recovery sequence is used (Arnold 2007; Nicasy et al. 2022). The experimental results, plotted in Fig. 10, indicate that all samples have a  $T_1$  relaxation time between 250 and 350 ms. As is mentioned in Sect. 2.2, the repetition time in experiments should be at least 4 times as high as the longest  $T_1$  relaxation time to ensure a sufficiently high signal. Here this means that a repetition time of at least 1.4 s should be used during experiments on  $\text{K}_2\text{CO}_3$  packed beds.

Transversal relaxation times of the calibration samples are measured via the CPMG sequence with an echo time of 250  $\mu\text{s}$  (Brown et al. 2014). In the measurements presented in Fig. 11, it is found that the  $T_2$  relaxation times consist out of two components which have different timescales and intensities. Measurements on an empty polypropylene sample holder are found to give results that are very similar to those of a completely dehydrated calibration sample: The relaxation times found are  $T_{2,1} = 0.46 \pm 0.05$  ms and  $T_{2,2} = 5 \pm 3$  ms with signal intensities  $S_1 = 11.2 \pm 0.7$  a.u. and  $S_2 = 0.6 \pm 0.4$  a.u. respectively.

Investigating the measurement results, it can be argued that  $T_{2,2}$  is most probably originating from the polypropylene sample holder that was used for the measurements. After all, the signal intensity  $S_2$  is approximately constant in all measurements and coincides with the value found for an empty sample holder. The signal intensity  $S_1$ , belonging to the short relaxation component, also corresponds to that of an empty sample holder when an anhydrous sample is measured. Increasing the loading of the calibration samples, it is however found to scale linearly with sample loading. Furthermore, the relaxation times  $T_{2,1}$  are found to lie in the range of relaxation times that were previously found by Donkers et al. to belong to structural or lattice water in different types of salt hydrates (Donkers et al. 2016,

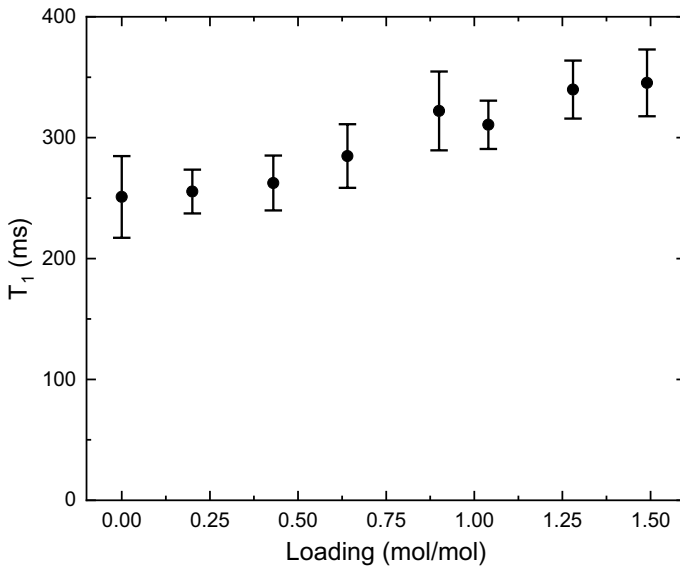


**Fig. 10** Plot of the  $T_1$  relaxation times, measured as a function of sample loading in mol  $H_2O$  per mol  $K_2CO_3$

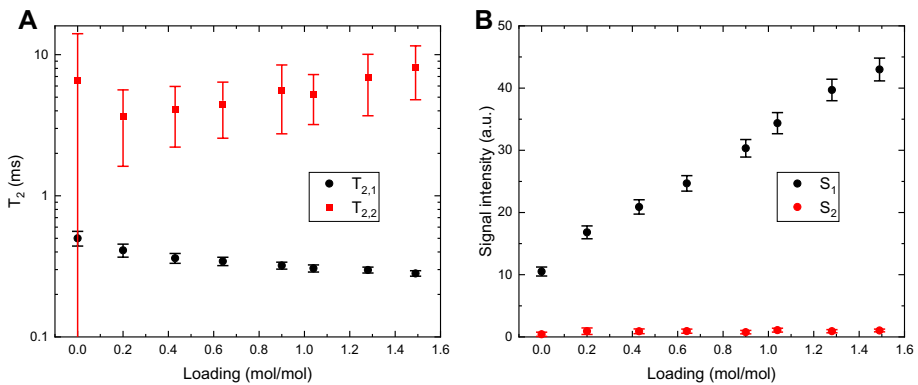


**Fig. 11** **A** Plot of the  $T_2$  relaxation times a function of sample loading in mol  $H_2O$  per mol  $K_2CO_3$ . **B** Plot of the intensities belonging to the different  $T_2$  relaxation components

2015). It can therefore be argued that the increasing intensity of this relaxation component must originate from the protons inside the  $K_2CO_3$  material.

**Acknowledgements** The authors would like to thank Jef Noijen, Hans Dalderop and Martijn Kurvers for their technical support and Ginny Fransen for the manufacturing of the Teflon reactor used in the NMR measurements.

**Author contributions** TR contributed to Conceptualization, Data curation, Formal analysis, Investigation, Methodology, Writing—original draft, Visualization. PD contributed to Conceptualization, Investigation, Methodology, Supervision, Writing—review & editing. HH contributed to Conceptualization, Funding acquisition, Project administration, Supervision, Writing—review & editing.

**Funding** This project has received funding from the European Unions Horizon 2020 research and innovation program under grant agreement No 869810. This work reflects only the author's view. The European Commission is not responsible for any use that may be made of this information.

**Data availability** The datasets generated during this study are available from the corresponding author on reasonable request.

## Declarations

**Conflict of interest** The authors declare that they have no known competing financial interests or personal relationships that could have appeared to influence the work reported in this paper. The authors declare the following financial interests/personal relationships which may be considered as potential competing interests.

**Open Access** This article is licensed under a Creative Commons Attribution 4.0 International License, which permits use, sharing, adaptation, distribution and reproduction in any medium or format, as long as you give appropriate credit to the original author(s) and the source, provide a link to the Creative Commons licence, and indicate if changes were made. The images or other third party material in this article are included in the article's Creative Commons licence, unless indicated otherwise in a credit line to the material. If material is not included in the article's Creative Commons licence and your intended use is not permitted by statutory regulation or exceeds the permitted use, you will need to obtain permission directly from the copyright holder. To view a copy of this licence, visit <http://creativecommons.org/licenses/by/4.0/>.

## References

- Aarts, J., de Jong, S., Cotti, M., Donkers, P., Fischer, H., Adan, O., Huinink, H.: Diffusion limited hydration kinetics of millimeter sized salt hydrate particles for thermochemical heat storage. *J. Energy Storage*. **47**, 103554 (2022). <https://doi.org/10.1016/j.est.2021.103554>
- Arnold, J.: Mobile NMR for rock porosity and permeability, <https://publications.rwth-aachen.de/record/49898>, (2007)
- Aydin, D., Casey, S.P., Riffat, S.: The latest advancements on thermochemical heat storage systems. *Renew. Sustain. Energy Rev.* **41**, 356–367 (2015). <https://doi.org/10.1016/j.rser.2014.08.054>
- Beving, M.A.J.M., Frijns, A.J.H., Rindt, C.C.M., Smeulders, D.M.J.: Effect of cycle-induced crack formation on the hydration behaviour of K<sub>2</sub>CO<sub>3</sub> particles: experiments and modelling. *Thermochim. Acta*. **692**, 178752 (2020). <https://doi.org/10.1016/j.tca.2020.178752>
- Beving, M., Romme, J., Donkers, P., Frijns, A., Rindt, C., Smeulders, D.: Experimental and numerical validation of the one-process modeling approach for the hydration of K<sub>2</sub>CO<sub>3</sub> particles. *Processes*. **10**, 547 (2022). <https://doi.org/10.3390/pr10030547>
- Brown, R.W., Cheng, Y.N., Haacke, E.M., Thompson, M.R., Venkatesan, R.: *Magnetic resonance imaging*. John Wiley & Sons Ltd, Chichester, UK (2014)
- Clark, R.-J., Mehrabadi, A., Farid, M.: State of the art on salt hydrate thermochemical energy storage systems for use in building applications. *J. Energy Storage*. **27**, 101145 (2020). <https://doi.org/10.1016/j.est.2019.101145>
- Criado, Y.A., Alonso, M., Abanades, J.C.: Kinetics of the CaO/Ca(OH)<sub>2</sub> hydration/dehydration reaction for thermochemical energy storage applications. *Ind. Eng. Chem. Res.* **53**, 12594–12601 (2014). <https://doi.org/10.1021/ie404246p>
- Donkers, P.A.J., Linnow, K., Pel, L., Steiger, M., Adan, O.C.G.: Na<sub>2</sub>SO<sub>4</sub>·10H<sub>2</sub>O dehydration in view of thermal storage. *Chem. Eng. Sci.* **134**, 360–366 (2015). <https://doi.org/10.1016/j.ces.2015.05.028>
- Donkers, P.A.J., Pel, L., Adan, O.C.G.: Experimental studies for the cyclability of salt hydrates for thermochemical heat storage. *J. Energy Storage*. **5**, 25–32 (2016). <https://doi.org/10.1016/j.est.2015.11.005>
- Donkers, P.A.J., Pel, L., Adan, O.C.G.: Dehydration/hydration of granular beds for thermal storage applications: a combined NMR and temperature study. *Int. J. Heat Mass Transf.* **105**, 826–830 (2017a). <https://doi.org/10.1016/j.jheatmasstransfer.2016.10.041>
- Donkers, P.A.J., Sögütoglu, L.C., Huinink, H.P., Fischer, H.R., Adan, O.C.G.: A review of salt hydrates for seasonal heat storage in domestic applications. *Appl. Energy*. **199**, 45–68 (2017b). <https://doi.org/10.1016/j.apenergy.2017.04.080>
- Gerber, G., Weitz, D.A., Coussot, P.: Propagation and adsorption of nanoparticles in porous medium as traveling waves. *Phys. Rev. Res.* (2020). <https://doi.org/10.1103/PhysRevResearch.2.033074>

- Goldstein, M.: Some physical chemical aspects of heat storage. In: UN Conference on New Sources of Energy. pp 411–417 (1961)
- Greenspan, L.: Humidity Fixed Points of Binary Saturated Aqueous Solutions. Journal of research of the national Bureau of Standards—A. Phys. Chem. **81**, 89–96 (1977)
- Houben, J., Sögütöglu, L., Donkers, P., Huinink, H., Adan, O.:  $K_2CO_3$  in closed heat storage systems. Renew. Energy. **166**, 35–44 (2020). <https://doi.org/10.1016/j.renene.2020.11.119>
- Huinink, H., de Jong, S., Houben, V.: Hydration fronts in packed particle beds of salt hydrates: Implications for heat storage. J Energy Storage. **71**, 108158 (2023). <https://doi.org/10.1016/j.est.2023.108158>
- Nicasy, R., Huinink, H., Erich, B., Olaf, A.: NMR profiling of reaction and transport in thin layers: a review. Polymers (basel) **14**, 798 (2022). <https://doi.org/10.3390/polym14040798>
- Scapino, L., Zondag, H.A., van Bael, J., Diriken, J., Rindt, C.C.M.: Sorption heat storage for long-term low-temperature applications: a review on the advancements at material and prototype scale. Appl. Energy. **190**, 920–948 (2017). <https://doi.org/10.1016/j.apenergy.2016.12.148>
- Sensirion: Datasheet SHT85 Humidity and Temperature Sensor, [https://sensirion.com/media/documents/4B40CEF3/61642381/Sensirion\\_Humidity\\_Sensors\\_SHT85\\_Datasheet.pdf](https://sensirion.com/media/documents/4B40CEF3/61642381/Sensirion_Humidity_Sensors_SHT85_Datasheet.pdf) (2021)
- SolarPower Europe: Global Market Outlook For Solar Power 2022–2026. (2022)
- Solé, A., Martorell, I., Cabeza, L.F.: State of the art on gas–solid thermochemical energy storage systems and reactors for building applications. Renew. Sustain. Energy Rev. **47**, 386–398 (2015). <https://doi.org/10.1016/j.rser.2015.03.077>
- Sögütöglu, L.-C., Birkelbach, F., Werner, A., Fischer, H., Huinink, H., Adan, O.: Hydration of salts as a two-step process: water adsorption and hydrate formation. Thermochim. Acta. **695**, 178819 (2021). <https://doi.org/10.1016/j.tca.2020.178819>
- Sögütöglu, L.C., Donkers, P.A.J., Fischer, H.R., Huinink, H.P., Adan, O.C.G.: In-depth investigation of thermochemical performance in a heat battery: cyclic analysis of  $K_2CO_3$ ,  $MgCl_2$  and  $Na_2S$ . Appl. Energy. **215**, 159–173 (2018). <https://doi.org/10.1016/j.apenergy.2018.01.083>
- Sögütöglu, L.-C., Steiger, M., Houben, J., Biemans, D., Fischer, H.R., Donkers, P., Huinink, H., Adan, O.C.G.: understanding the hydration process of salts: the Impact of a nucleation barrier. Cryst. Growth Des. **19**, 2279–2288 (2019). <https://doi.org/10.1021/acs.cgd.8b01908>

**Publisher's Note** Springer Nature remains neutral with regard to jurisdictional claims in published maps and institutional affiliations.

## Authors and Affiliations

Tim Raemaekers<sup>1</sup>  · Pim Donkers<sup>2</sup> · Henk Huinink<sup>1,3</sup> 

✉ Henk Huinink  
h.p.huinink@tue.nl

Tim Raemaekers  
t.l.e.m.raemaekers@tue.nl

Pim Donkers  
pim.donkers@cellcius.com

<sup>1</sup> Transport in Permeable Media Group, Department of Applied Physics, Eindhoven University of Technology, PO Box 513, 5600 MB Eindhoven, The Netherlands

<sup>2</sup> Cellcius, Horsten 1, 5612 AX Eindhoven, The Netherlands

<sup>3</sup> Eindhoven Institute of Renewable Energy Systems, Eindhoven University of Technology, PO Box 513, 5600 MB Eindhoven, The Netherlands